Acta Materialia 227 (2022) 117727

Contents lists available at ScienceDirect

Acta Materialia

journal homepage: www.elsevier.com/locate/actamat

Quench rate sensitivity of age-hardenable Al-Zn-Mg-Cu alloys with respect to the Zn/Mg ratio: An *in situ* SAXS and HEXRD study

Gloria Graf[a], Petra Spoerk-Erdely[a,*], Peter Staron[b], Andreas Stark[b], Francisca Mendez Martin[a], Helmut Clemens[a], Thomas Klein[c]

[a] *Department of Materials Science, Montanuniversität Leoben, Franz Josef-Straße 18, 8700 Leoben, Austria*
[b] *Helmholtz-Zentrum Hereon, Institute of Materials Physics, Max-Planck-Straße 1, 21502 Geesthacht, Germany*
[c] *LKR Light Metals Technologies Ranshofen, Austrian Institute of Technology, Lamprechtshausener Straße 61, 5282 Ranshofen, Austria*

ARTICLE INFO

Article history:
Received 28 September 2021
Revised 3 February 2022
Accepted 6 February 2022
Available online 7 February 2022

Keywords:
Al-Zn-Mg-Cu
Aluminum alloys
Synchrotron radiation
Quench sensitivity
Precipitation

ABSTRACT

Al-Zn-Mg-Cu alloys with a low Zn/Mg ratio have attracted considerable attention in recent years as a result of an attractive property portfolio based on their ability of age hardening via the precipitation of the T-$Mg_{32}(Al,Zn)_{49}$ phase and its precursors. In this study, the quench rate sensitivity of an Al-Mg-Zn-Cu alloy with low Zn/Mg ratio is investigated and compared to a commercial reference Al-Zn-Mg-Cu alloy (AA7075) showing a high Zn/Mg ratio. The impact of five different cooling rates in the range of 0.25–100 K/s on the precipitation of quench-induced particles was studied by means of *in situ* small-angle X-ray scattering and high-energy X-ray diffraction. Subsequent continuous annealing experiments showed the influence of the cooling rate on the precipitation of fine hardening phases. Selected heat treatment conditions were further studied via scanning electron microscopy and atom probe tomography in order to reveal the microstructure and the chemical composition of the T-$Mg_{32}(Al,Zn)_{49}$ precipitates. The results showed that the Al-Mg-Zn-Cu alloy with low Zn/Mg ratio exhibits a lower quench rate sensitivity than the commercial AA7075 alloy. The lowest cooling rates, at which no quench-induced precipitation occurs, are in the range of 1 K/s for the investigated Al-Mg-Zn-Cu alloy and 100 K/s for the AA7075 alloy. The robust precipitation behavior of the Al-Mg-Zn-Cu alloy with a low Zn/Mg ratio is expected to be beneficial for advanced manufacturing processes.

© 2022 The Author(s). Published by Elsevier Ltd on behalf of Acta Materialia Inc.
This is an open access article under the CC BY license (http://creativecommons.org/licenses/by/4.0/)

1. Introduction

Al-Zn-Mg-Cu alloys belong to the AA7xxx series aluminum alloys, which show the highest strengths amongst aluminum base alloys and are, thus, widely applied in the aircraft industry [1]. Their excellent mechanical performance is achieved via age hardening, *i.e.* the precipitation of nm-scaled metastable phases from a supersaturated solid solution (SSSS). In AA7xxx alloys, typically a high Zn/Mg ratio is adjusted. For these alloys, the precipitation sequence during aging from a SSSS is generally accepted as [2]: SSSS → Guinier-Preston (GP) zones → η' → η (space group $P6_3/mmc$; lattice constants $a = 5.15$ Å and $c = 8.48$ Å [3]), with a recent study suggesting the formation of an additional intermediate phase between the η' and the η phase [4].

In recent years, alloys with a low Zn/Mg ratio have attracted considerable attention [5–14], based on their hardenability via precipitation of the T-$Mg_{32}(Al,Zn,Cu)_{49}$ phase (space group $Im\bar{3}m$; lattice constant $a = 14.16$ Å [15]) and its precursors [5]. These alloys are often referred to as “crossover alloys”, as they merge alloy systems beyond the borders of conventional systems [11,12]. This single-alloy approach also improves their recyclability [16]. The precipitation sequence of alloys with a low Zn/Mg ratio, as proposed by Hou et al. [10], is SSSS → GPI zone → GPII zone → intermediate phase T' → equilibrium phase T-$Mg_{32}(Al,Zn)_{49}$. Various age hardening studies have already been conducted in order to optimize heat treatment procedures [8,10,11]. These works have shown that the age hardening response can be enhanced and accelerated through an additional pre-aging step, which also alters the precipitation sequence. Stemper et al. [12] have highlighted that the addition of Cu can further increase the hardening potential and thus reduce the aging time.

---

[*] Corresponding author.

E-mail addresses: gloria.graf@unileoben.ac.at (G. Graf), petra.spoerk-erdely@unileoben.ac.at (P. Spoerk-Erdely), peter.staron@hereon.de (P. Staron), andreas.stark@hereon.de (A. Stark), francisca.mendez-martin@unileoben.ac.at (F. Mendez Martin), helmut.clemens@unileoben.ac.at (H. Clemens), thomas.klein@ait.ac.at (T. Klein).

https://doi.org/10.1016/j.actamat.2022.117727
1359-6454/© 2022 The Author(s). Published by Elsevier Ltd on behalf of Acta Materialia Inc. This is an open access article under the CC BY license (http://creativecommons.org/licenses/by/4.0/)

Table 1
Chemical compositions of the Al-Mg-Zn-Cu and the AA7075 alloy in m.% (at.%).

Alloy	Al	Zn	Mg	Cu	Mn	Si	Fe	Zr	Cr
Al-Mg-Zn-Cu	bal.	3.6 (1.51)	5.9 (6.66)	0.3 (0.13)	0.5 (0.25)	0.1 (0.10)	0.1 (0.05)	0.1 (0.03)	–
AA7075	bal.	5.87 (2.53)	2.46 (2.85)	1.6 (0.71)	0.04 (0.02)	0.1 (0.10)	0.2 (0.10)	–	0.2 (0.11)

Alloy systems of this kind have recently been considered as potential materials for additive manufacturing [13,14]. Since additively manufactured materials are not intended to be plastically deformed after the building process (except for a few process variants), an increase in hardness can only be achieved by subsequent age hardening. While conventional AA7xxx alloys with a high Zn/Mg ratio are prone to hot cracking [17,18], crack-free structures could be produced when the Mg content was increased [13,14] in accordance with an earlier work by Eskin et al. [19]. Alloys with a low Zn/Mg ratio, therefore, seem to be better suited for additive manufacturing.

In order to obtain the maximum strength via age hardening, the quenching step after the solution heat treatment is crucial. If the cooling rate is too low, coarse quench-induced precipitates can be formed [20,21]. On the one hand, they are too coarse to contribute to strengthening, and on the other hand, they decrease the content of main alloying elements in solid solution. Then the main alloying elements are not available for the formation of desired nm-scaled precipitates in a subsequent age hardening step. Consequently, a loss in hardness is observed [20,21]. A significant amount of research has been conducted on conventional alloy systems [20–23]. However, little is yet known about the quench rate sensitivity of Al-Zn-Mg-Cu alloys with a low Zn/Mg ratio and the concomitantly different precipitation reactions.

In this work, the quench rate sensitivity of an Al-Mg-Zn-Cu alloy with a low Zn/Mg ratio of 0.6 is investigated and compared to a conventional high strength AA7075 alloy with a high Zn/Mg ratio of 2.4. Small-angle X-ray scattering (SAXS) and high-energy X-ray diffraction (HEXRD) investigations have been conducted to trace the nature and dimension of precipitates in an *in situ* manner. After quenching at various cooling rates ranging from 0.25 to 100 K/s, the specimens have been continuously annealed in order to study the influence of the cooling rate on the precipitation behavior during annealing. Scanning electron microscopy (SEM) and atom probe tomography (APT) have been conducted on selected conditions to examine the microstructure and to determine the chemical composition of the T-$Mg_{32}(Al,Zn,Cu)_{49}$ phase.

2. Experimental

2.1. Material and processing

A conventional AA7075 alloy with a high Zn/Mg ratio of 2.4 and an alloy with a low Zn/Mg ratio of 0.6, which in the following will be referred to as “Al-Mg-Zn-Cu alloy”, are studied. Their chemical compositions were measured by means of optical emission spectroscopy with a SPECTROMAXx 6 from SPECTRO Analytical Instruments and are shown in Table 1.

Specimens of the Al-Mg-Zn-Cu alloy were machined from an ingot that was custom-fabricated via continuous vertical casting and uniaxially compressed to close residual porosity. Reference specimens of the AA7075 alloy were machined from commercially available plate material.

Fig. 1 illustrates the heat treatments conducted on the specimens during *in situ* SAXS and HEXRD. In a first step, the specimens were solution heat-treated at 500 °C for 20 min. The heating rate applied was 15 K/s. Subsequently, the samples were continuously cooled at 5 different cooling rates: 0.25 K/s, 1 K/s, 30 K/s, 50 K/s, and 100 K/s. To study the influence of these cooling rates on the precipitation behavior during annealing, the specimens were then continuously heated to a temperature of 400 °C at a rate of 0.167 K/s (10 K/min). Additionally, three *ex situ* samples (marked in Fig. 1 with blue dots) were prepared from each alloy for investigation by means of SEM. APT measurements were also performed on the *ex situ* samples of the Al-Mg-Zn-Cu alloy. The first two conditions consisted of the solution heat treatment followed by cooling at 100 K/s (C1) and 0.25 K/s (C2). The third heat treatment (C3) was slightly different for the two alloys. Alloy AA7075 was cooled at 0.25 K/s and then continuously annealed up to 265 °C at a heating rate of 0.167 K/s. After reaching 265 °C, the specimen was immediately quenched to room temperature at the highest rate possible with the dilatometer. The Al-Mg-Zn-Cu alloy was annealed up to only 255 °C. The low cooling rate was chosen due to its relevance for processing technologies. Further, at these annealing temperatures, the highest volume fractions of precipitates were identified by means of SAXS.

2.2. Scanning electron microscopy

In order to reveal the microstructure of the *ex situ* specimens in the heat-treated conditions (C1-C3 in Fig. 1) as well as the initial condition, SEM investigations were performed. For the heat treatments, cylindrical specimens with a diameter of 5 mm and a length of 10 mm were mounted in a dilatometer DIL 805 A by TA Instruments. For temperature control, a type S thermocouple was spot-welded onto the sample surface. N_2 was utilized as quenching gas. The heat-treated samples as well as samples in the initial condition were cold-mounted in Demotec 70 to prevent the formation of precipitates during the mounting process. Afterward, the mounted specimens were ground with SiC-paper of different grain sizes and polished with diamond suspension of 3 µm and 1 µm. The final step was chemo-mechanical polishing with colloidal silica. The SEM investigation was then performed with a Clara Tescan in back-scatter electron (BSE) mode at a voltage of 15 keV. Additionally, energy-dispersive X-ray spectroscopy (EDX) measurements were conducted with an Oxford Instruments X-Max EDS system to qualitatively reveal the chemical composition of the phases present in the alloys.

2.3. Synchrotron experiments

The *in situ* SAXS and HEXRD experiments were conducted at the Deutsches Elektronen-Synchrotron (DESY) in Hamburg, Germany. The beamline used was the high-energy materials science (HEMS) beamline P07, operated by Helmholtz-Zentrum Hereon at PETRA III. A mean photon energy of 70 keV ($\lambda = 0.177$ Å) was chosen. Cylindrical specimens with a diameter of 5 mm and a length of 10 mm were mounted inside a modified dilatometer DIL 805A/D by TA Instruments to perform the heat treatments. The temperature was traced with the aid of a type S thermocouple spot-welded onto the specimen surface. During the heat treatments, which were operated under Ar atmosphere, the specimens were continually probed in transmission geometry.

2.3.1. High-energy X-ray diffraction

For the *in situ* HEXRD measurements a PerkinElmer (PE) XRD 1621 flat panel detector with a total number of pixels of 2048 × 2048 and a pixel size of 200 × 200 μm^2 was utilized.

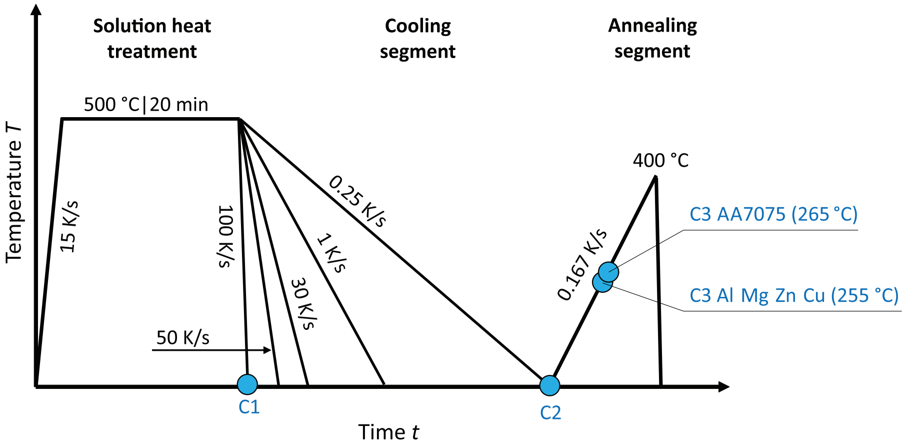

Fig. 1. Scheme of heat treatments applied during *in situ* SAXS and HEXRD measurements. Following the solution treatment, specimens were cooled at 5 different cooling rates and subsequently continuously annealed. C1, C2 and C3 are the *ex situ* conditions investigated by means of SEM (and APT in the case of the Al-Mg-Zn-Cu alloy). Condition C3 was cooled at a rate of 0.25 K/s.

The detector was situated centrically to allow the detection of the full Debye-Scherrer rings. The distance from specimen to detector was 1567 mm and the setup was calibrated using LaB_6. During the solution and annealing treatment, the detector dwell time equaled 10 s. During the cooling segment of the heat treatment, it was reduced to 1 s, except for the slowest cooling rate (0.25 K/s), for which also 10 s were used. Diffraction patterns were generated by azimuthally integrating the detector images with the aid of the software Fit2D [24].

2.3.2. Small-angle X-ray scattering

A PE XRD 1621 flat panel detector was placed centrically at a distance of 10,078 mm from the specimen to capture the scattered X-rays. A beamstop with a diameter of 200 µm was employed and the setup was calibrated with silver behenate. The same detector frame rates as for the HEXRD experiments were applied for the SAXS experiments. As the scattering signal was isotropic, the scattering curves were obtained by azimuthally integrating the detector signal. The scattering curves were corrected for transmission and the background was subtracted with an air measurement. This was performed using the software Fit2D [24]. The macroscopic scattering cross-section was calibrated with glassy carbon [25].

In order to trace the precipitation process as a function of time, the scattering curves were integrated to calculate the integrated intensity Q according to Eq. (1):

$$Q = 4\pi \int_{q_{min}=0}^{q_{max}=\infty} \frac{d\Sigma}{d\Omega}(q) q^2 dq. \tag{1}$$

In this work, the macroscopic differential scattering cross-section $d\Sigma/d\Omega$ was only integrated between q-values of 0.1 and 0.5 nm^{-1}, with q being the magnitude of the scattering vector. Thus, the integrated intensity will be referred to as Q' in the following. To determine the mean radius and the particle volume fraction qualitatively, the scattering curves were fitted with the in-house software SANSFit, using lognormal particle distributions [26]. On the basis of the APT measurements, a scattering contrast of 8.74×10^{10} cm^{-2} was calculated for the T-$Mg_{32}(Al,Zn,Cu)_{49}$ phase in the Al-Mg-Zn-Cu alloy. The chemical composition of the η'/η precipitates in the AA7075 alloy was estimated as 35.3 at.% Al, 35.4 at.% Zn, 26.2 at.% Mg and 3.1 at.% Cu based on recent findings by Wang et al. [27], who conducted similar heat treatments. Thus, the scattering contrast for the AA7075 alloy was assumed to be 1.069×10^{11} cm^{-2}. In other investigations of similar alloys, the chemical compositions of precipitates are in the range of 33–58 at.% Al, 22–37 at.% Zn, 15–27 at.% Mg and 1–8 at.% Cu [27–32]. For the fit of both alloys, the scattering contrast was set constant during the heat treatment and the particles were assumed to be spherical. It should be mentioned that a scattering signal was detected at a temperature of 500 °C after a holding time of 20 min (*i.e.* the starting condition before the quenching experiment), which was probably generated by larger undissolved phases. This constant signal was assumed to be background. Therefore, only the contribution of precipitates newly formed during the quenching and annealing segments was considered in this investigation.

2.4. Atom probe tomography

Heat treatments as described in Section 2.2. were performed to investigate the chemical composition of the precipitates formed in the Al-Mg-Zn-Cu alloy. Rods with a quadratic cross-section were prepared from the heat-treated samples with an Accutom-5R from Struers GmbH. These rods were then mounted in a copper holder and in a first step, electrolytically polished with a 5% perchloric acid in acetic acid to produce a rough tip. In a second step, a fine tip with a radius of about 50–100 nm was created using a 2% perchloric acid in butoxyethanol. The APT specimens were then measured in a local electrode atom probe (LEAP^{TM}) 3000X HR from Cameca Instruments Inc. at a temperature of 50 K. Voltage mode was applied with a pulse frequency of 200 kHz and a pulse fraction of 20%. The chemical composition of the precipitates and the matrix was evaluated using the Cameca IVAS^{TM} 3.6.8 software package.

3. Results and discussion

3.1. Microstructure

Fig. 2(a) shows the SEM micrograph of the Al-Mg-Zn-Cu alloy in the initial condition prior to the heat treatment. Coarse precipitates and microsegregation zones located at the grain boundaries of α-Al grains are visible. One fraction of the coarse precipitates displays a lighter contrast than the α-Al matrix. EDX measurements disclosed that these precipitates comprise Mn- and Fe-rich phases as well as Mg-, Zn- and Cu-rich phases. The other fraction shows a darker contrast and represents Mg- and Si-rich particles. This is in good agreement with the types of precipitates found by Klein et al. [13] in wire and arc additively manufactured samples of the same alloy. An EDX mapping, which is shown Fig. S1

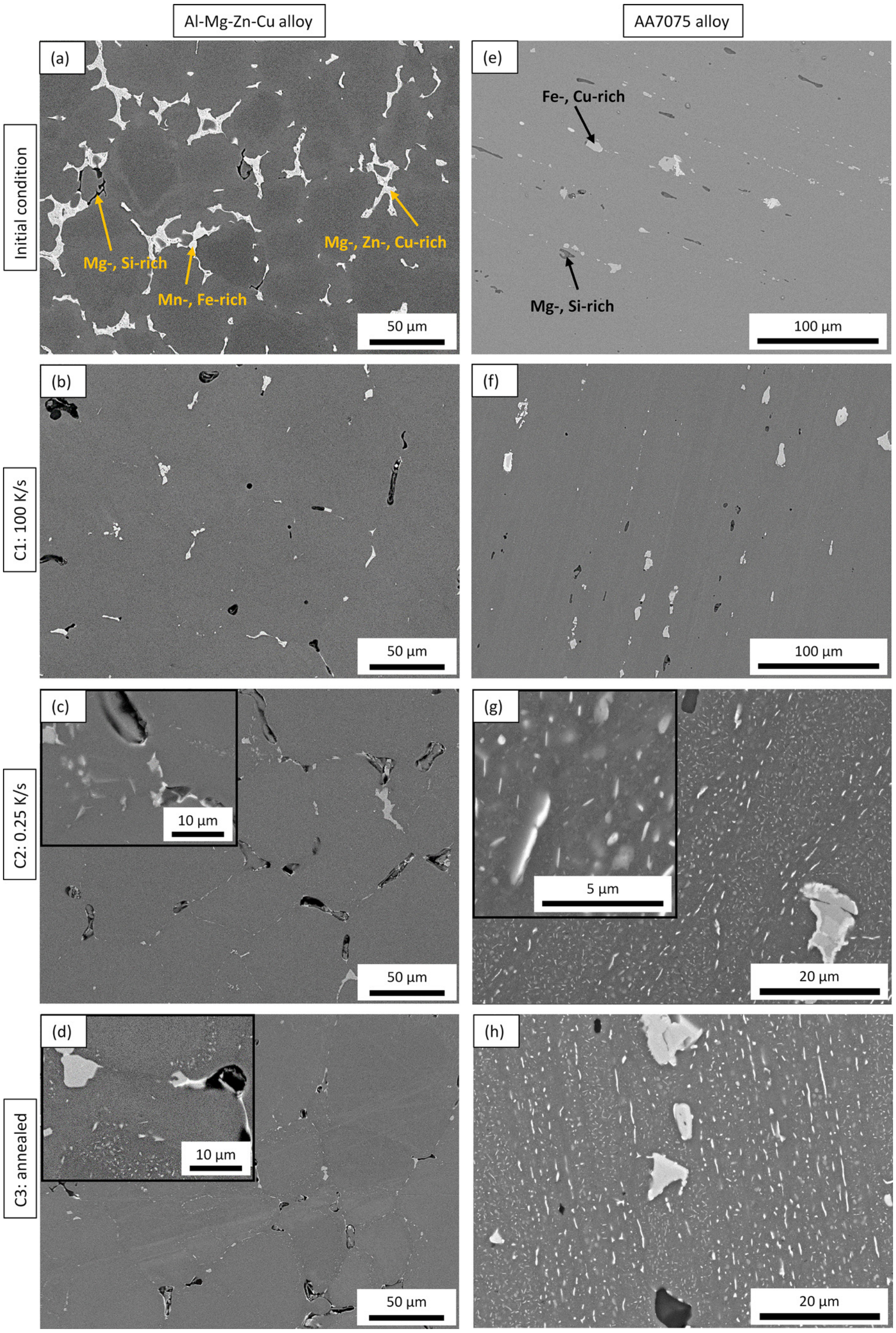

Fig. 2. SEM micrographs of the Al-Mg-Zn-Cu alloy (a)-(d) and the AA7075 alloy (e)-(h). Displayed are the initial conditions (a) and (e), the conditions cooled at 100 K/s (C1) (b) and (f), the conditions cooled 0.25 K/s (C2) (c) and (g), and the conditions annealed at 255 °C (d) and 265 °C (h) (C3). All images are taken in BSE mode.

in the supplementary data, also revealed that alloying elements such as Mg, Zn or Cu tend to segregate to the vicinity of the grain boundaries, causing the slightly lighter contrast in the SEM image near the grain boundaries. Segregations like these are known to be formed during solidification due to an enrichment of solute atoms in the liquid phase and insufficient diffusion in the solid phase [33].

Fig. 2(b) illustrates the microstructure of the Al-Mg-Zn-Cu alloy in condition C1 (see Fig. 1). The Mg-, Zn- and Cu-rich phases completely dissolve during the solution treatment. As confirmed by EDX point measurements, only the Mn- and Fe-rich phases and Mg- and Si-rich phases are retained at the α-Al grain boundaries. These phases typically remain stable up to the liquidus temperature as recently assessed by Dinsdale et al. [34]. At this high cooling rate, no particles can be found in the matrix due to the limited resolution.

In Fig. 2(c), the sample cooled at a rate of 0.25 K/s is depicted. Similar to Fig. 2(b), only the coarse Fe- and Mn-rich and Mg- and Si-rich grain boundary precipitates still remain after the solution treatment. As a result of the slow cooling rate, however, additional smaller precipitates, which are enriched in Zn and Mg, have formed along the grain boundaries. In the matrix, fine Zn- and Mg-rich phases are located near the grain boundaries, but are not found in the center, as can be seen in the magnified inset. The formation of precipitates near the grain boundaries is caused by the locally increased amount of alloying elements due to segregation, as described above. Additionally, a higher diffusivity near the grain boundaries can be assumed [35]. HEXRD measurements proved the

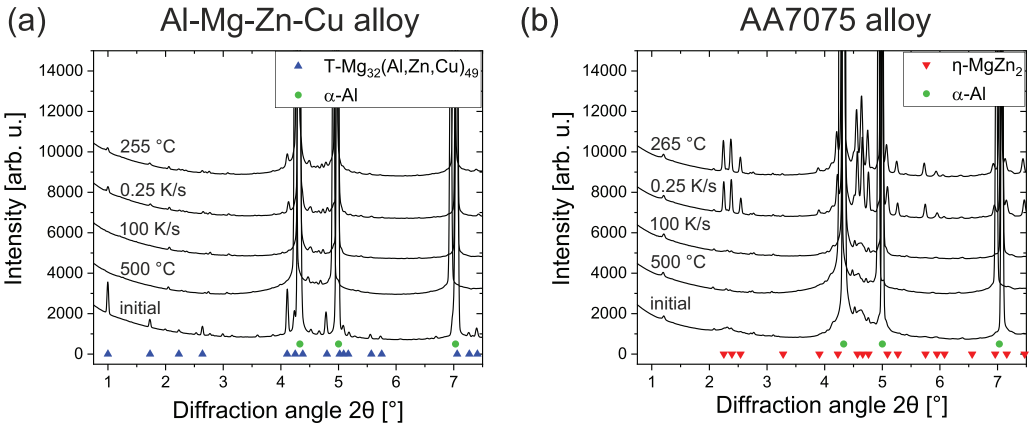

Fig. 3. *In situ* HEXRD diffraction patterns of the Al-Mg-Zn-Cu alloy (a) and the AA7075 alloy (b). Diffraction patterns of the initial condition, the last frame taken during the solution treatment at 500 °C, the conditions cooled at 100 K/s and 0.25 K/s, respectively, and the condition cooled at 0.25 K/s and annealed to 255 °C in (a) and 265 °C in (b) are shown. Please note the slight shift in the peak positions resulting from the temperature changes during the *in situ* experiment.

identity of the Zn- and Mn-rich phases to be T-$Mg_{32}(Al,Zn,Cu)_{49}$ or its precursors (see Section 3.2). Since there are no significant differences between the crystal structures of the T-$Mg_{32}(Al,Zn,Cu)_{49}$ phase and its precursors [10,36], a further distinction between these phases is not attempted in the present study.

The Al-Mg-Zn-Cu specimen in the C3 condition is shown in Fig. 2(d). In this sample, the amount of fine T-$Mg_{32}(Al,Zn,Cu)_{49}$ phase precipitates located in the vicinity of the grain boundaries has increased compared to the sample shown in Fig. 2(c).

In Fig. 2(e), the SEM micrograph of the AA7075 alloy in the initial condition is illustrated. The microstructure is banded and consists of elongated matrix grains alongside coarse elongated dark and light contrasted phases. EDX point measurements revealed that the dark phases are Mg- and Si-rich precipitates. The phases showing a light contrast are enriched in Fe and Cu. No precipitates were found in the matrix.

Fig. 2(f) depicts the AA7075 specimen in C1 condition. As in the initial condition, coarse phases appear in a banded alignment and no precipitates are present in the matrix.

The SEM micrograph of the AA7075 specimen in C2 condition is displayed in Fig. 2(g). Coarse light and dark contrasted phases are still present in the microstructure. However, compared to the specimen cooled at 100 K/s, new precipitates with a light contrast and dimensions in the range of a few micrometers have formed during the slow cooling process. The precipitates in the microstructure appear aligned – a result of the previous processing steps. Some of the precipitates are elongated, others spherical, see magnified inset. EDX measurements suggest that those phases are enriched in Mg and Zn and should thus be η-$Mg(Zn,Al,Cu)_2$ phase or its precursors [27,31,32].

Fig. 2(h) presents a SEM image of a specimen in C3 condition. The microstructure consists of coarse phases with light and dark contrast and fine phases with light contrast, comparable to the microstructure shown in Fig. 2(g). Some of the elongated precipitates have grown and increased their aspect ratio.

3.2. High-energy X-ray diffraction

Fig. 3 displays the *in situ* HEXRD diffraction patterns corresponding to the conditions discussed in the previous chapter, plus one additional condition per alloy at the end of the solution treatment at 500 °C. In Fig. 3(a), the pattern for the Al-Mg-Zn-Cu alloy is shown. A high volume fraction of T-$Mg_{32}(Al,Zn,Cu)_{49}$ phase is already visible in the initial condition, implying that this corresponds to the Mg-, Zn- and Cu-rich grain boundary phase found in Fig. 2(a). After the solution heat treatment at 500 °C, the T-$Mg_{32}(Al,Zn,Cu)_{49}$ phase is completely dissolved. Its formation is further completely suppressed at a cooling rate of 100 K/s. However, after slower cooling at 0.25 K/s, the formation of T-$Mg_{32}(Al,Zn,Cu)_{49}$ phase is again clearly discernible, and its volume fraction further increases in the course of the ensuing continuous aging to a temperature of 255 °C. This behavior is consistent with the SEM investigation, which proved that smaller Mg- and Zn-rich precipitates appear in the vicinity of the grain boundaries (Figs. 2(c) and (d)). Thus, it is evident that the hardening phase in the Al-Mg-Zn-Cu alloy with low Zn/Mg ratio investigated here is the T-$Mg_{32}(Al,Zn,Cu)_{49}$ phase and its precursors, in agreement with literature [10]. Additionally, small amounts of Mg_2Si, Al_6Mn and Al_7Cu_2Fe are present, which are commonly found in Al-Zn-Mg-Cu alloys [13,37,38].

HEXRD diffraction patterns of the AA7075 alloy are shown in Fig. 3(b). The main hardening phase in this alloy is based on η-$Mg(Zn,Al,Cu)_2$ and its precursors [2,39]. In the initial condition (Fig. 3(b)), a small fraction of η-$Mg(Zn,Al,Cu)_2$ phase is present, which is completely dissolved prior to the quenching segment after the 20 min solution treatment at 500 °C. Quenching at 100 K/s leads to the formation of only a small fraction of η-$Mg(Zn,Al,Cu)_2$ phase, whereas after cooling at 0.25 K/s the peaks of the η-$Mg(Zn,Al,Cu)_2$ phase are clearly discernible. The subsequent annealing to a temperature of 265 °C does not significantly alter the phase fraction of the precipitate phase. These HEXRD findings compare well with the SEM investigation. In a more detailed evaluation of minor phases, Al_7Cu_2Fe, Mg_2Si and Al_6Mn were identified. Some kind of cubic Fe-rich phase, such as $Al_{12}(Fe,Mn)_3Si$ [40] or $Al_{19}Fe_4MnSi_2$ [34], which can often be found in AA7xxx alloys, might also be present.

3.3. Atom probe tomography

Since the existence range of the T-$Mg_{32}(Al,Zn)_{49}$ phase in the ternary Al-Mg-Zn system is very broad [41], its chemical composition in the Al-Mg-Zn-Cu alloy was determined via APT in order to calculate the scattering length density difference. Table 2 displays the chemical composition of the conditions C1-C3. In comparison to the material's global chemical composition shown in Table 1, a reduced level of alloying elements such as Mg, Zn and Cu is present in the matrix of the C1 condition. The reduction in alloying elements may be ascribed to their segregation to the vicinity of the grain boundaries as can be seen in Fig. 2(a) and the corresponding EDX maps in Fig. S1. Since the grain boundary area was the first to be dissolved during the preparation of the specimens via electrolytic polishing, the APT measurements were performed

Table 2
Chemical compositions (in at.%) of matrix and T-$Mg_{32}(Al,Zn,Cu)_{49}$ phase in the Al-Mg-Zn-Cu alloy for conditions cooled at 100 K/s (C1), 0.25 K/s (C2) and cooled at 0.25 K/s and subsequently annealed to 255 °C (C3) as derived from APT analyses (see text).

Heat treatment	Phase	Al	Zn	Mg	Cu	Mn	Zr	Cr	Fe
C1	matrix	93.51	1.22	4.89	0.04	0.25	0.05	0.03	0.00
C2	matrix	93.94	1.04	4.63	0.03	0.24	0.06	0.04	0.00
C3	matrix	95.29	0.53	3.96	0.10	0.10	0.02	0.01	0.00
C3	T-phase	48.42	18.37	31.74	0.71	0.11	0.00	0.00	0.66

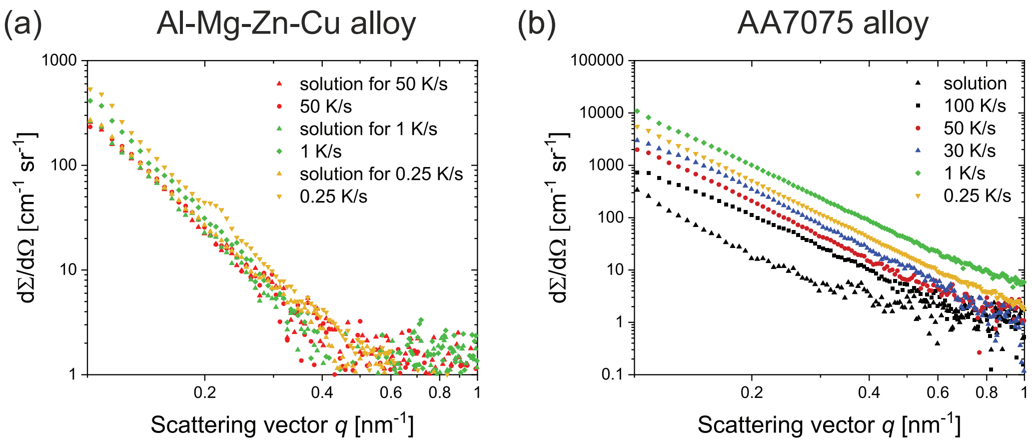

Fig. 4. Scattering curves recorded for the Al-Mg-Zn-Cu alloy (a) and the AA7075 alloy (b). The figure compares the last frame taken during the solution treatment at 500 °C with the scattering curves captured at room temperature after cooling at the given rates.

in the grain center. Thus, the segregated amount of alloying elements might not be captured in the measurement. Additionally, Mg_2Si phases are present in the microstructure, as shown by SEM and HEXRD, which further reduce the Mg content in the matrix.

During slow cooling at 0.25 K/s (C2), T-$Mg_{32}(Al,Zn,Cu)_{49}$ phase precipitates are formed, further reducing the content of Zn, Mg and Cu in the matrix [42]. Even though the presence of these precipitates was detectable via HEXRD as well as SEM, they were not captured during the APT measurements. Hence, their chemical composition is not listed in Table 2. As can be seen in the SEM investigation, the precipitates are formed in the vicinity of the grain boundaries (see Fig. 2(c)), which dissolved first during preparation. This might be the reason that precipitates are not visible in the APT measurements.

A further depletion of alloying elements in the matrix is distinguishable in condition C3. Here the precipitate density was high enough to capture the T-$Mg_{32}(Al,Zn,Cu)_{49}$ phase during APT measurements. Chemical compositions for the T'/T-phase in single-step aged material [8,36] are comparable with the composition given in Table 2. With APT measurements, Cao et al. [8] found approximately 42 at.% Al, 17 at.% Zn, 39 at.% Mg, and 2 at.% Cu, and Bigot et al. [36] found 36.5 at.% Al, 26 at.% Zn,and 37.5 at.% Mg. The results in this work are close to the equilibrium composition in the Al-Mg-Zn ternary phase diagram in Ref. [41] as well.

3.4. Small-angle X-ray scattering

3.4.1. Cooling segments

In Fig. 4, scattering curves captured at the beginning as well as at the end of the respective cooling segments are visible. Fig. 4(a) visualizes the results on the Al-Mg-Zn-Cu alloy. Being representative for the high cooling rates, *i.e.* 100 K/s, 50 K/s and 30 K/s, only the sample cooled at 50 K/s is illustrated, in order to avoid unnecessary clutter of the data. As can be seen in Fig. S2, the scattering curves of specimens cooled at rates ≥30 K/s display no significant difference from the condition at 500 °C. Consequently, the formation of quench-induced particles is suppressed during fast cooling. However, as can be observed in Fig 4(a) a significant change occurs in the SAXS signal for specimens cooled at rates ≤1 K/s. The scattering curves shift to higher intensity values with decreasing cooling rates in comparison to the starting condition. A distinct shoulder is not visible, indicating the presence of coarse particles larger than 20 nm, which cannot be resolved with the used SAXS setup. Therefore, the mean radius of the particles cannot be determined, but a shift of the scattering curve to higher intensities suggests an increase in volume fraction of the coarse particles.

Fig. 4(b) illustrates the scattering curves of the AA7075 alloy. The specimens cooled at different cooling rates all show an increased scattering signal with respect to the reference condition at 500 °C, implying that quench-induced particles are present even after cooling rates of 100 K/s. This is in contrast to the results of the Al-Mg-Zn-Cu alloy, in which quench-induced precipitates are only observed at the two lowest cooling rates. Additionally, a small shoulder is visible in the scattering curve after cooling at 100 K/s, which is shifted to smaller *q*-values for lower cooling rates. Consequently, particles within the detected *q*-range with a mean radius of 7–10 nm are present after cooling. However, their particle size distribution is anticipated to be rather broad, since the shoulder is very broad as well. With decreasing cooling rates, larger precipitates are detected, as longer durations at high temperatures provide increased atomic mobility. At the two lowest cooling rates (≤1 K/s), the shoulder has shifted outside of the detected *q*-range. Furthermore, a higher volume fraction of precipitates is present with decreasing cooling rate. The exception is the specimen cooled at 0.25 K/s, which, in contrast to the Al-Mg-Zn-Cu alloy, does not show the highest intensity values. Rietveld analysis of the precipitate phase fraction was conducted on the HEXRD signal of the specimens cooled at 1 K/s and 0.25 K/s after the cooling segment and no significant difference is discernible. A possible reason for this finding is that the volume fraction of the precipitates in the two specimens is similar, and the particles in the specimen cooled at 0.25 K/s are already coarser. With increasing particle radius, the scattering curve is shifted toward smaller *q*-values so that the detected SAXS signal appears artificially reduced.

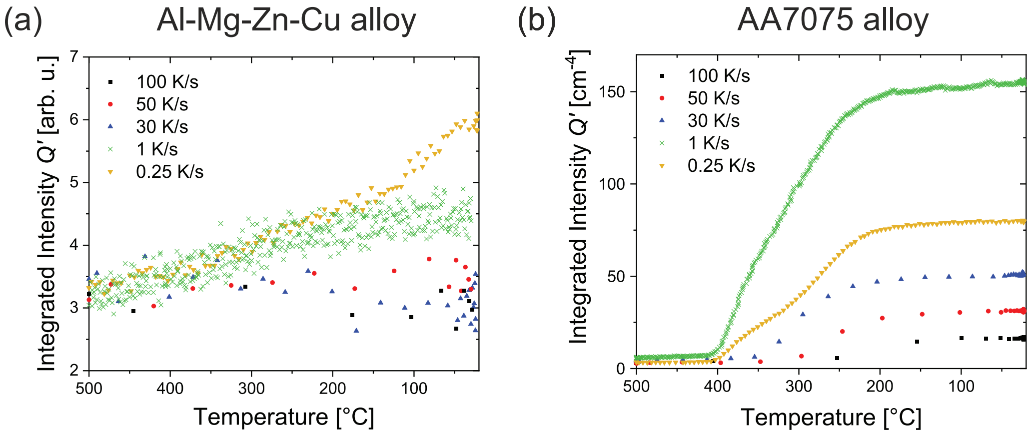

Fig. 5. Development of the integrated intensity Q' during cooling of the Al-Mg-Zn-Cu alloy (a) and the AA7075 alloy (b) at five different rates. For reasons of improved visibility, the curves have been normalized and shifted to the same starting point in (a). In this case, Q' is therefore given in arbitrary units.

In both investigated alloys, an increase in volume fraction of quench-induced precipitates with decreasing cooling rate is apparent, and in the AA7075 alloy an increase in precipitate radius with decreasing cooling rate is noticeable as well. An equivalent behavior was reported by Zhang et al. [23] in their investigation of the quench rate sensitivity of different Al-Zn-Mg-Cu alloys. With lower cooling rates both the volume fraction and the Guinier Radius of the quench-induced precipitates increased. In their investigation, the quench-induced particles were also comparably large with a Guinier Radius $R_g > 17$ nm, underpinning our previous argumentation.

To trace the precipitation behavior during the cooling segments, the integrated intensity Q' was calculated for both alloys in a q-range of 0.1–0.5 nm^{-1} (Fig. 5). The Q'-value increases with increasing volume fraction of the particles and increasing scattering contrast. The latter depends on the chemical composition of the matrix and precipitates. Fig. 5(a) visualizes the precipitation behavior in the Al-Mg-Zn-Cu alloy during five different cooling segments. The results shown in this figure compare well with Fig. 4(a). During cooling at the three highest cooling rates, the Q'-values remain mostly constant, *i.e.* no precipitation takes place within the detectable q-range. In the specimens that were cooled at 1 K/s and 0.25 K/s, Q' rises continuously starting from around 460 °C. This temperature is consistent with the calculated equilibrium solution temperature of the T-$Mg_{32}(Al,Zn,Cu)_{49}$ phase in this alloy and thus supports previous thermodynamic calculations reported by Klein et al. [13]. While for the specimen cooled at 1 K/s the rate of change in Q' seems to decrease at around 200 °C, diffusional processes including precipitation and growth proceed until room temperature for the specimen cooled at 0.25 K/s.

Fig. 5(b) displays the integrated intensity Q' for five different cooling rates for the AA7075 alloy. Pronounced variations with respect to the cooling rate are observed. With decreasing cooling rate, the value of Q' increases, *i.e.* the volume fraction of precipitates rises, with exception of the specimen cooled at 0.25 K/s. As already mentioned the volume fraction of precipitates in the specimens cooled at 1 K/s and 0.25 K/s is comparable, however, the precipitates in the specimen cooled at 0.25 K/s are already coarser. Due to the shift of the shoulder to smaller q-values the signal appears artificially reduced. The onset of precipitation in the specimen cooled at the lowest rate is at approximately 400 °C and shifts to lower temperatures with increasing cooling rates corresponding to an increased nucleation supercooling. Additionally, Q' reaches a plateau value for all cooling rates below around 200 °C, suggesting a freeze out of particle growth. The starting and finishing temperatures of precipitation are in good agreement with the values reported by Milkereit et al. [43] for the equivalent cooling rates in a AA7075 alloy.

3.4.2. Continuous annealing segments

In Fig. 6, selected scattering curves for the annealing segments of the two alloys are compared, displaying exemplarily the specimens cooled at 100 K/s. Most specimens showed a clearly discernible and continually shifting shoulder. It should be noted, however, that precipitation during annealing of the AA7075 alloy was hardly visible for specimens cooled at 1 K/s and 0.25 K/s, *i.e.* the shoulder in the scattering curve was very small.

Fig. 6(a) illustrates the scattering curves of the Al-Mg-Zn-Cu alloy. While no shoulder is observable at ambient temperature, a shoulder resulting from the formation of particles is apparent already at 200 °C. With increasing temperature, the formed particles grow and the shoulder shifts to smaller q-values and eventually out of the detected q-range at around 350 °C. At 400 °C the volume fraction of the T-$Mg_{32}(Al,Zn,Cu)_{49}$ phase precipitates decreases due to the onset of particle dissolution (see also the following figures and thermodynamic calculations of Ref. [13]).

A similar behavior can be observed in Fig. 6(b) for the AA7075 alloy. At 170 °C a shoulder is clearly visible in the scattering curve, which is shifted to smaller q-values with increasing temperature, indicating first the formation and subsequently the growth of precipitates. Those are eventually dissolved at temperatures above 350 °C when the scattering signal decreases almost to the starting condition again.

Since clear shoulders are apparent in most SAXS datasets during the annealing segment, the mean radius and volume fraction of the particles can be obtained via fitting the data. In Figs. 7(a) and (b), the mean radius and volume fraction of particles precipitated during annealing of the Al-Mg-Zn-Cu specimen cooled at 100 K/s can be seen. Starting from 165 °C, the volume fraction increases as first precipitates are formed. Subsequently to the precipitation onset, particle growth prevails and the radius and volume fraction of precipitates increase with increasing temperature. At a temperature of 260 °C, the volume fraction starts to decrease and particles begin to dissolve, but coarsening further proceeds. Above a temperature of 315 °C, open symbols are used in Figs. 7(a) and (b) to express that the shoulder in the scattering curve has shifted out of the detected q-range, thus affecting the accuracy of the fitting procedure. The behavior shown in Figs. 7(a) and (b) compares well with differential scanning calorimetry (DSC) measurements by Klein et al. [13].

In Fig. 7(c) and (d) the AA7075 specimen cooled at 100 K/s is illustrated. Here, a different behavior can be observed for the

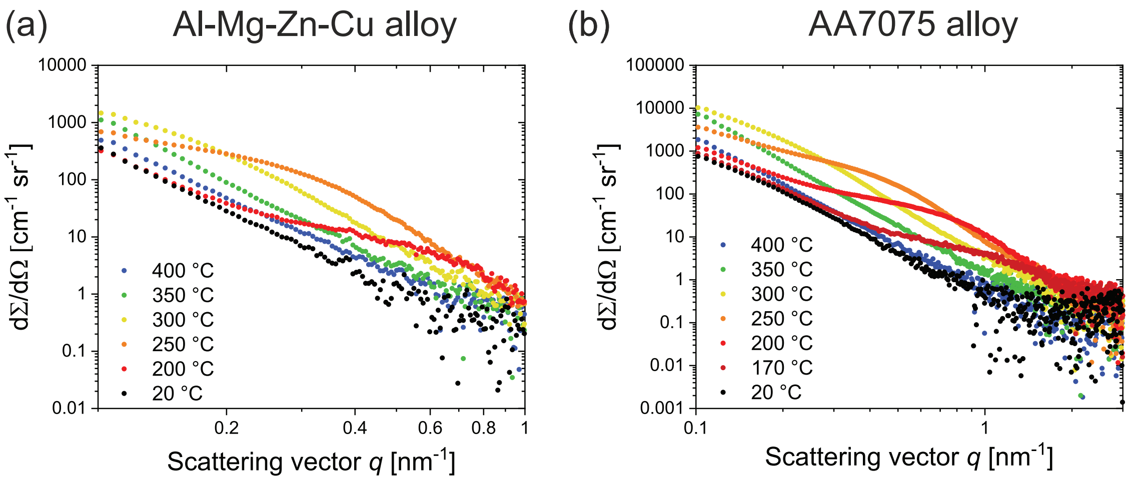

Fig. 6. Selected scattering curves of the Al-Mg-Zn-Cu alloy (a) and the AA7075 alloy (b) recorded during annealing after cooling at 100 K/s.

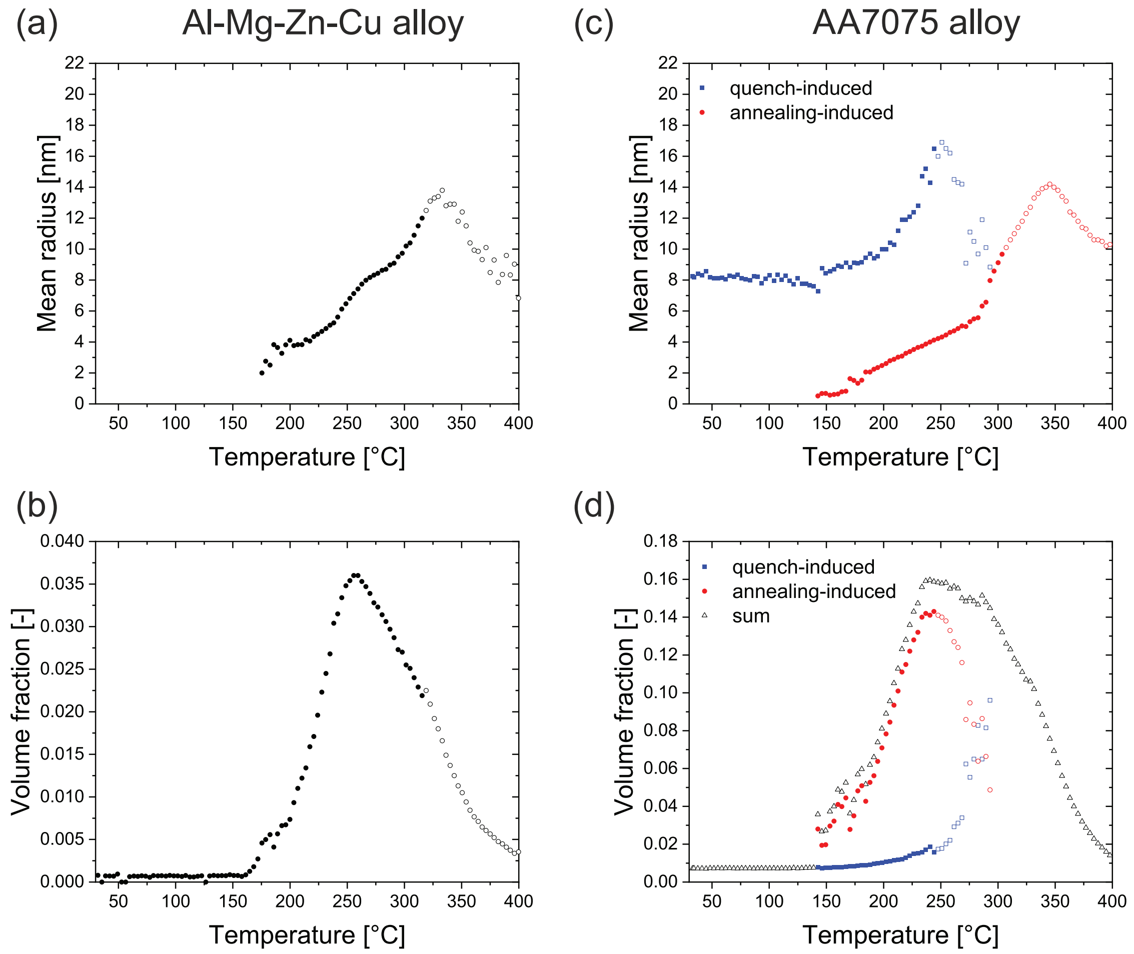

Fig. 7. Mean radius and volume fraction of precipitates formed during continuous annealing in the Al-Mg-Zn-Cu alloy (a)-(b) and the AA7075 alloy (c)-(d). Both alloys were cooled at a rate of 100 K/s after the solution treatment. The heating rate during annealing was 0.167 K/s. Open symbols are used after the shoulder shifted out of the detected *q*-range in the scattering curves in order to indicate that the fit might not accurately represent the radius and volume fraction.

particle radius and volume fraction. Two different size distributions of particles predominate – a larger and a smaller one (see Fig. 7(c)). The larger one represents quench-induced particles. The smaller one corresponds to particles, which are newly formed during the annealing segment. Precipitation of the newly formed particles starts at around 145 °C. The onset of growth of quench-induced particles is noticeable at around the same temperature, suggesting that the kinetics of both processes are governed by the diffusion of equivalent chemical species. The phase fraction of the sum of both populations peaks at around 245 °C and subsequently decreases as the precipitates dissolve. This temperature fits well to

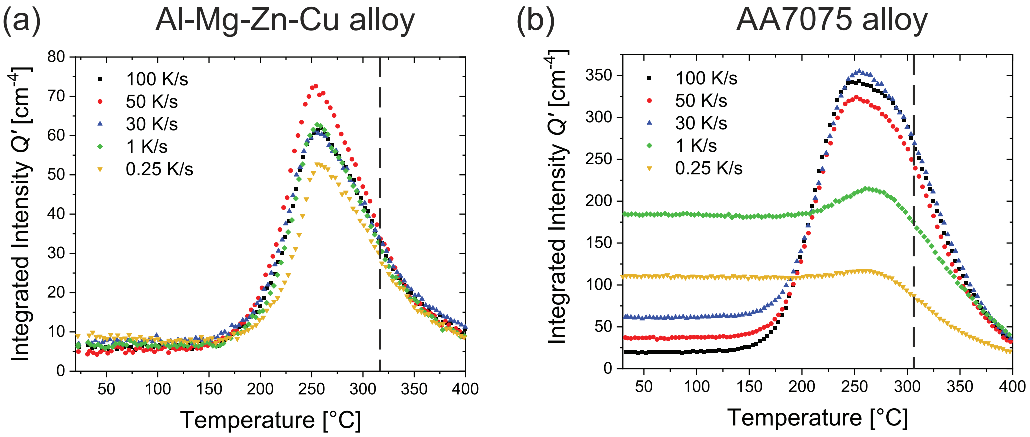

Fig. 8. Development of the integrated intensity *Q'* during continuous annealing of the Al-Mg-Zn-Cu alloy (a) and the AA7075 alloy (b) at a heating rate of 0.167 K/s. As indicated, the specimens have previously been cooled at different rates. The dashed line represents the temperature from which the shoulder shifted out of the detected *q*-range. Note that the ordinates of (a) and (b) are scaled differently.

data determined by Österreicher et al. [44] using DSC. At 400 °C, all the precipitates are dissolved again.

The behavior of both alloys upon quenching and annealing is similar to the one found by Zhang et al. [23], who suggested the prevalence of three particle distributions: A coarse one originating from quench-induced precipitates, a medium-sized distribution within a *q*-range of 0.2–2 nm^{-1} assigned to precipitates formed during annealing and a small-sized distribution. The latter is believed to be GP zones, which evolve during natural aging. Due to the immediate annealing step after the solution treatment, no natural aging occurred in the present investigation.

Fig. 8 shows the integrated intensity *Q'* measured during the annealing segments of the two alloys. In Fig. 8(a), the annealing segments are displayed for the Al-Mg-Zn-Cu alloy. Generally, the precipitation behavior of the specimens cooled previously at different rates appears similar. At around 150 °C, the integrated intensity starts to increase. Diffusion of alloying elements at this point is fast enough to trigger the growth of precipitates. Precipitation proceeds up to a temperature of approximately 255 °C, where *Q'* reaches a peak value. With further heating, precipitates start to dissolve again, indicated by the decreasing integrated intensity. Equivalent behavior is observed irrespective of the previous cooling rate. However, the specimen cooled at 50 K/s displays a higher peak and the specimen cooled at 0.25 K/s a lower peak than the other three specimens. Moreover, the *Q'* value at the beginning of the annealing segment is slightly lower in the specimen cooled at 50 K/s. Thus, the volume fraction of coarse phases may be correspondingly lower. Hence, alloying elements, which would otherwise be bound by the coarse phases, are therefore available in the matrix resulting in an increased amount of precipitates during annealing. The specimen initially cooled at 0.25 K/s on the contrary has a higher *Q'* starting value due to the presence of T-$Mg_{32}(Al,Zn,Cu)_{49}$ phase after the long cooling period (see Fig. 5(a)). As seen in Section 3.4.1., these phases are too large to be measured within the *q*-range probed and consequently mostly newly formed fine precipitates influence the *Q'* value. Since the formation of quench-induced precipitates depletes the matrix of alloying elements, less alloying elements are available for the formation of new precipitates during annealing, explaining the smaller peak of the specimen cooled at 0.25 K/s.

In contrast to the Al-Mg-Zn-Cu alloy, in which the behavior during annealing is largely unaffected by the preceding cooling rate, the precipitation behavior in the AA7075 alloy during annealing is strongly dependent on the cooling rate after the solution heat treatment. This is shown in Fig. 8(b), in which the evolution of the integrated intensity *Q'* with temperature is displayed. For cooling rates ≥30 K/s, the precipitation behavior during annealing is similar. It starts with a rise in *Q'* at around 125–150 °C and reaches a peak value at approximately 260 °C. The different *Q'* values at the beginning of the annealing segment do not have an influence on the peak height, since the number of particles formed after the previous cooling segment is comparably small for these three cooling rates. After reaching the peak value, *Q'* decreases again and, consequently, also the phase fraction of precipitates.

Specimens which were cooled at rates up to 1 K/s show a different behavior upon annealing (see Fig. 8(b)). The annealing segment already starts with a high *Q'* value, indicative for the presence of quench-induced phases. The matrix is, thus, largely depleted in precipitate forming alloying elements [23,42]. The onset of newly formed particles is therefore shifted to higher temperatures, *i.e.* 200 °C and 225 °C for cooling rates of 1 K/s and 0.25 K/s, respectively. This observation is in agreement with Robson [45], who provided a theoretic framework for the dependence of the nucleation rate, growth and coarsening on the matrix supersaturation. Furthermore, the peak correlated to precipitation is not as pronounced as for higher cooling rates and its height is significantly lower. As the amount of alloying elements available in the matrix is smaller, also a smaller volume fraction of new precipitates can be formed. This is also observable in the scattering curves, in which the shoulder belonging to newly formed particles is hardly visible. After reaching the peak value at a temperature of approximately 265 °C, particles eventually start to dissolve irrespective of the previous cooling rate and the presence or absence of quench-induced precipitates.

3.5. Quench rate sensitivity and its technological implications

From the *in situ* SAXS quenching and annealing experiments, it is apparent that the Al-Mg-Zn-Cu alloy exhibits a lower quench rate sensitivity than the AA7075 alloy. In the Al-Mg-Zn-Cu alloy quench-induced precipitates were only detected at extremely low cooling rates ≤1 K/s. Even though precipitation during cooling was already observed at a rate of 1 K/s, the phase fraction was apparently too low at this cooling rate to have a significant influence on the precipitation behavior during the subsequent annealing step, since the same volume fraction was formed during annealing as for rates ≥30 K/s (see Fig. S3). Even at a cooling rate of 0.25 K/s a relatively low volume fraction of quench-induced precipitates was present after cooling, so that in turn the formation of fine-scaled particles upon annealing almost reached the same level as for rapidly cooled specimens with rates ≥1 K/s. In contrast to the Al-Mg-Zn-Cu alloy, the quench-induced precipitation in the AA7075 alloy cannot be suppressed for cooling rates ≤100 K/s and increases with decreasing cooling rate. Nonetheless, the precipitation during quenching for cooling rates ≥30 K/s does not seem to have a strong influence on the precipitation behavior upon annealing. For cooling rates ≤1 K/s, though, almost no fine precipitates are formed during annealing.

Quench rate sensitivity is a complex phenomenon, especially in AA7xxx alloys due to the multiple potential combinations of alloying elements [20]. Upon quenching, different types of coarse phases can form, which do not contribute to the strengthening, but instead decrease the amount of alloying elements in solid solution for the formation of fine hardening phases. Quench rate sensitivity usually increases with increasing content of main alloying elements, but also depends on the chemical composition in general and the concentration of dispersoid-forming alloying elements [20,21]. The density of nucleation sites, *e.g.* dislocations, grain boundaries, dispersoids, coarse primary particles or undissolved secondary phases, further has a considerable influence [20,21]. Generally, AA7xxx alloys show a higher quench rate sensitivity compared to other aluminum-based alloying systems due to their high alloying content [20]. Critical cooling rates, *i.e.* the lowest cooling rate at which no precipitation occurs, are in the range of 3–300 K/s for AA7xxx alloys. The AA7075 alloy lies in the upper range of the spectrum with a critical cooling rate of 100–300 K/s [20,22,43], which is consistent with the results in this investigation. The Al-Mg-Zn-Cu alloy investigated in this study has a very low critical cooling rate in the order of 1 K/s.

As mentioned above, the quench rate sensitivity commonly increases with increasing alloying content. Even though the Al-Mg-Zn-Cu alloy has a relatively high alloying content (in at.%) compared to the AA7075 alloy, it still has a lower quench sensitivity than AA7075. Liu et al. [22] also reported that, although AA7075 has a lower alloying content compared to other AA7xxx alloys, it has yet a higher quench rate sensitivity. This behavior was explained with a higher content of incoherent dispersoids, which enhance the quench rate sensitivity by acting as nucleation sites [21,22]. When Cr is included as a trace element, incoherent Cr-rich dispersoids are formed and might act as nucleation sites in alloys like AA7075 [22]. Another type of dispersoid is the Al_3Zr-phase, which is usually coherent to the matrix and in that case not effective as a nucleation site [21]. If the material recrystallizes, Al_3Zr dispersoids become incoherent and heterogeneous nucleation of quench-induced particles can take place as described in Ref. [21,46]. Since the Al-Mg-Zn-Cu alloy contains Zr and was produced via casting without working, dispersoids are not expected to have a high impact on the quench rate sensitivity. It is, however, possible that they play a role in the Cr-containing AA7075 alloy, in which they enhance the precipitation kinetics. It was further found that a higher Cu content and a lower Zn/Mg ratio leads to a higher quench sensitivity in commercial AA7xxx alloys, which have hardening phases based on η-Mg(Zn,Al,Cu)$_2$ and its precursors [20,22,23]. These elements favor the formation of S-Al_2CuMg phase at higher temperatures, which decreases the amount of alloying elements in the matrix [47]. Nonetheless, no S phase was identified in either of the alloys investigated in the present work. The tendency reported with respect to the Zn/Mg ratio is in line with the present results of AA7075. In case of the AA7075 alloy, the low Zn/Mg ratio compared to other commercial AA7xxx alloys and moderate amounts of Cu each contribute to a high quench rate sensitivity.

Regarding the technological aspects, the quench rate sensitivity has a high impact on the mechanical properties of the final product. Hence, the manufacturing process has to be adjusted accordingly. In the case of the Al-Mg-Zn-Cu alloy investigated in this work, its low quench rate sensitivity has a positive effect on the processability of the alloy. The robustness against deviating cooling conditions is, for example, beneficial for thick-walled components, since the center of the structure cools at lower rates after the solution heat treatment. Premature precipitation and the resulting loss of hardness in the core can therefore be avoided. Due to the lower cooling rates, which can be applied, processing via high pressure die casting or extrusion of the Al-Mg-Zn-Cu alloy may be possible as well. Furthermore, its low quench rate sensitivity is essential for new processing techniques like additive manufacturing, in which an intrinsic heat treatment is applied during the production of the component [48,49]. The heat influence of the deposition of subsequent layers provokes the precipitation of coarse phases in quench rate sensitive alloys, depleting the matrix [49]. In the layers close to the substrate, the depletion of the matrix causes a reduction of solid solution strengthening, leading to a structural part with anisotropic mechanical properties. A previous investigation showed a sturdier behavior after the additive manufacturing process of the Al-Mg-Zn-Cu alloy used in this work, which can be explained due to the low quench rate sensitivity [48]. It is also worth noting that the Al-Mg-Zn-Cu alloy exhibits rather high yield strengths in comparison to other age-hardenable aluminum alloys, which show comparable quench rate sensitivities [13,20,50,51]. Especially components designed for lightweight applications would benefit from these improved mechanical properties as well as the robust quenching behavior.

4. Conclusions

In this study, *in situ* SAXS and HEXRD experiments were performed to investigate the quench rate sensitivity of two Al-Zn-Mg-Cu alloys with high and low Zn/Mg ratio. Furthermore, SEM and APT experiments have been conducted corroborating our understanding of the *in situ* experiments. From the analyses performed the following major conclusions can be drawn:

- In the case of the alloy with low Zn/Mg ratio, the phase precipitated during cooling and subsequent annealing is the T-Mg_{32}(Al,Zn,Cu)$_{49}$ phase or its precursors, whereas in the case of the alloy with a high Zn/Mg ratio it is the η-Mg(Zn,Al,Cu)$_2$ phase or its precursors.
- The chemical composition of the T-Mg_{32}(Al,Zn,Cu)$_{49}$ phase in the alloy with low Zn/Mg ratio was determined as 48.4 at.% Al, 18.4 at.% Zn, 31.7 at.% Mg, and 0.7 at.% Cu.
- With decreasing cooling rate, the radius and volume fraction of coarse quench-induced particles increases. This increasing volume fraction of quench-induced precipitates results in turn in a reduction of the volume fraction of fine precipitates formed during annealing.
- The alloy with the high Zn/Mg ratio shows a much higher quench rate sensitivity than the alloy with low Zn/Mg ratio. The critical cooling rate for which no precipitation occurs during cooling is in the order of 100 K/s for the alloy with a high Zn/Mg ratio and 1 K/s for the alloy with a low Zn/Mg ratio.
- Upon continuous annealing, a reduced formation of precipitates is observed for the alloy with low Zn/Mg ratio at a cooling rate of 0.25 K/s. The cooling rate for which no precipitation occurs during annealing is not within the range of the investigated cooling rates. In the alloy with a high Zn/Mg ratio, the formation of particles during continuous annealing does not seem to be reduced for cooling rates ≥30 K/s. Almost no precipitation during annealing is found for cooling rates around 0.25 K/s.
- The absence of quench-induced precipitation over widely varying cooling conditions in the alloy with a low Zn/Mg ratio suggests robust processability during advanced processing technologies such as various additive manufacturing techniques. Irrespec-

tive of previous cooling conditions, nearly equivalent precipitation responses are observed.

Declaration of Competing Interest

The authors declare that they have no known competing financial interests or personal relationships that could have appeared to influence the work reported in this paper.

Acknowledgements

This research was funded within the AIT's strategic research portfolio 2021. We acknowledge DESY (Hamburg, Germany), a member of the Helmholtz Association HGF, for the provision of experimental facilities at PETRA III. The beamline P07 (HEMS) is operated by Helmholtz-Zentrum Hereon and we would like to thank Norbert Schell and Emad Maawad for assistance in using the beamline and dilatometer. Beamtime was allocated for proposal I-20190932 EC. The research leading to this result has been supported by the project CALIPSOplus under the Grant Agreement 730872 from the EU Framework Programme for Research and Innovation HORIZON 2020.

Supplementary materials

Supplementary material associated with this article can be found, in the online version, at doi:10.1016/j.actamat.2022.117727.

References

[1] I. Polmear, D. StJohn, J.-F. Nie, M. Qian, Light Alloys: Metallurgy of the Light Metals, Butterworth-Heinemann, 2017.
[2] H. Löffler, I. Kovács, J. Lendvai, Decomposition processes in Al-Zn-Mg alloys, J. Mater. Sci. 18 (1983) 2215–2240.
[3] J.B. Friauf, The crystal structure of magnesium di-zincide, Phys. Rev. 29 (1927) 34–40.
[4] J.Z. Liu, J.H. Chen, X.B. Yang, S. Ren, C.L. Wu, H.Y. Xu, J. Zou, Revisiting the precipitation sequence in Al–Zn–Mg-based alloys by high-resolution transmission electron microscopy, Scr. Mater. 63 (2010) 1061–1064.
[5] X.B. Yang, J.H. Chen, J.Z. Liu, F. Qin, J. Xie, C.L. Wu, A high-strength AlZnMg alloy hardened by the T-phase precipitates, J. Alloys Compd. 610 (2014) 69–73.
[6] C. Cao, Di Zhang, Z. He, L. Zhuang, J. Zhang, Enhanced and accelerated age hardening response of Al-5.2Mg-0.45Cu (wt%) alloy with Zn addition, Mater. Sci. Eng. A 666 (2016) 34–42.
[7] C. Cao, Di Zhang, X. Wang, Q. Ma, L. Zhuang, J. Zhang, Effects of Cu addition on the precipitation hardening response and intergranular corrosion of Al-5.2Mg-2.0Zn (wt.%) alloy, Mater. Charact. 122 (2016) 177–182.
[8] C. Cao, Di Zhang, L. Zhuang, J. Zhang, Improved age-hardening response and altered precipitation behavior of Al-5.2Mg-0.45Cu-2.0Zn (wt%) alloy with pre-aging treatment, J. Alloys Compd. 691 (2017) 40–43.
[9] S. Hou, Di Zhang, Q. Ding, J. Zhang, L. Zhuang, Solute clustering and precipitation of Al-5.1Mg-0.15Cu-xZn alloy, Mater. Sci. Eng. A 759 (2019) 465–478.
[10] S. Hou, P. Liu, Di Zhang, J. Zhang, L. Zhuang, Precipitation hardening behavior and microstructure evolution of Al-5.1 Mg-0.15Cu alloy with 3.0Zn (wt%) addition, J. Mater. Sci. 53 (2018) 3846–3861.
[11] L. Stemper, B. Mitas, T. Kremmer, S. Otterbach, P.J. Uggowitzer, S. Pogatscher, Age-hardening of high pressure die casting AlMg alloys with Zn and combined Zn and Cu additions, Mater. Des. 181 (2019) 107927.
[12] L. Stemper, M.A. Tunes, P. Oberhauser, P.J. Uggowitzer, S. Pogatscher, Age-hardening response of AlMgZn alloys with Cu and Ag additions, Acta Mater 195 (2020) 541–554.
[13] T. Klein, M. Schnall, B. Gomes, P. Warczok, D. Fleischhacker, P.J. Morais, Wire-arc additive manufacturing of a novel high-performance Al-Zn-Mg-Cu alloy: processing, characterization and feasibility demonstration, Addit. Manuf. 37 (2021) 101663.
[14] P.J. Morais, B. Gomes, P. Santos, M. Gomes, R. Gradinger, M. Schnall, S. Bozorgi, et al., Characterisation of a high-performance Al-Zn-Mg-Cu alloy designed for wire arc additive manufacturing, Materials (Basel) 13 (2020).
[15] G. Bergman, J.L.T. Waugh, L. Pauling, The crystal structure of the metallic phase Mg32(Al, Zn)49, Acta Crystallogr 10 (1957) 254–259.
[16] D. Raabe, C.C. Tasan, E.A. Olivetti, Strategies for improving the sustainability of structural metals, Nature 575 (2019) 64–74.
[17] R. Casati, M. Coduri, M. Riccio, A. Rizzi, M. Vedani, Development of a high strength Al–Zn–Si–Mg–Cu alloy for selective laser melting, J. Alloys Compd. 801 (2019) 243–253.
[18] N. Kaufmann, M. Imran, T.M. Wischeropp, C. Emmelmann, S. Siddique, F. Walther, Influence of process parameters on the quality of aluminium alloy EN AW 7075 using selective laser melting (SLM), Phys. Procedia 83 (2016) 918–926.
[19] D.G. Eskin, L.Katgerman Suyitno, Mechanical properties in the semi-solid state and hot tearing of aluminium alloys, Prog. Mater. Sci. 49 (2004) 629–711.
[20] B. Milkereit, M.J. Starink, P.A. Rometsch, C. Schick, O. Kessler, Review of the quench sensitivity of aluminium alloys: analysis of the kinetics and nature of quench-induced precipitation, Materials (Basel) 12 (2019).
[21] M.J. Starink, B. Milkereit, Y. Zhang, P.A. Rometsch, Predicting the quench sensitivity of Al–Zn–Mg–Cu alloys: a model for linear cooling and strengthening, Mater. Des. 88 (2015) 958–971.
[22] S. Liu, Q. Zhong, Y. Zhang, W. Liu, X. Zhang, Y. Deng, Investigation of quench sensitivity of high strength Al–Zn–Mg–Cu alloys by time–temperature-properties diagrams, Mater. Des. 31 (2010) 3116–3120.
[23] Y. Zhang, D. Pelliccia, B. Milkereit, N. Kirby, M.J. Starink, P.A. Rometsch, Analysis of age hardening precipitates of Al-Zn-Mg-Cu alloys in a wide range of quenching rates using small angle X-ray scattering, Mater. Des. 142 (2018) 259–267.
[24] A.P. Hammersley, S.O. Svensson, M. Hanfland, A.N. Fitch, D. Hausermann, Two-dimensional detector software: from real detector to idealised image or two-theta scan, High Press. Res 14 (1996) 235–248.
[25] A.J. Allen, F. Zhang, R.J. Kline, W.F. Guthrie, J. Ilavsky, NIST standard reference material 3600: absolute intensity calibration standard for small-angle x-ray scattering, J. Appl. Crystallogr. 50 (2017) 462–474.
[26] P. Staron, U. Christoph, F. Appel, H. Clemens, SANS investigation of precipitation hardening of two-phase γ-TiAl alloys, Appl. Phys. A Mater. Sci. Process. 74 (2002) s1163–s1165.
[27] Y. Wang, X. Wu, L. Cao, X. Tong, Y. Zou, Q. Zhu, S. Tang, et al., Effect of Ag on aging precipitation behavior and mechanical properties of aluminum alloy 7075, Mater. Sci. Eng. A 804 (2021) 140515.
[28] A. Bigot, F. Danoix, P. Auger, D. Blavette, A. Reeves, Tomographic atom probe study of age hardening precipitation in industrial AlZnMgCu (7050) alloy, Mater. Sci. Forum 217-222 (1996) 695–700.
[29] A. Deschamps, A. Bigot, F. Livet, P. Auger, Y. Bréchet, D. Blavette, A comparative study of precipitate composition and volume fraction in an Al–Zn–Mg alloy using tomographic atom probe and small-angle X-ray scattering, Philos. Mag. A 81 (2001) 2391–2414.
[30] G. Sha, A. Cerezo, Characterization of precipitates in an aged 7xxx series Al alloy, Surf. Interface Anal. 36 (2004) 564–568.
[31] S.-H. Gong, J.-Y. Lee, Y.-J. Kim, Atom-probe tomographic and electron microscopic analyses of a high strength 7075-T4 aluminum alloy, J. Nanosci. Nanotechnol. 19 (2019) 4182–4187.
[32] Y. Zhang, S. Jin, P.W. Trimby, X. Liao, M.Y. Murashkin, R.Z. Valiev, J. Liu, et al., Dynamic precipitation, segregation and strengthening of an Al-Zn-Mg-Cu alloy (AA7075) processed by high-pressure torsion, Acta Mater 162 (2019) 19–32.
[33] W. Kurz, D.J. Fisher, Fundamentals of Solidification, 4th ed., Trans Tech Publications, Uetikon-Zuerich, 2005.
[34] A. Dinsdale, C. Fang, Z. Que, Z. Fan, Understanding the thermodynamics and crystal structure of complex Fe containing intermetallic phases formed on solidification of aluminium alloys, JOM 71 (2019) 1731–1736.
[35] M. de Hass, J.T.M. de Hosson, Grain boundary segregation and precipitation in aluminium alloys, Scr. Mater. 44 (2001) 281–286.
[36] A. Bigot, P. Auger, S. Chambreland, D. Blavette, A. Reeves, Atomic scale imaging and analysis of T' precipitates in Al-Mg-Zn alloys, Microsc. Microanal. Microstruct. 8 (1997) 103–113.
[37] C. Walde, K. Tsaknopoulos, V. Champagne, D. Cote, Phase transformations in thermally treated gas-atomized Al 7075 powder, Metallogr. Microstruct. Anal. 9 (2020) 419–427.
[38] Y. Zhu, K. Sun, G.S. Frankel, Intermetallic phases in aluminum alloys and their roles in localized corrosion, J. Electrochem. Soc. 165 (2018) C807–C820.
[39] Y. Fan, X. Tang, S. Wang, B. Chen, Comparisons of age hardening and precipitation behavior in 7075 alloy under single and double-stage aging treatments, Met. Mater. Int. 7 (2020) 26.
[40] W. Yang, S. Ji, X. Zhou, I. Stone, G. Scamans, G.E. Thompson, Z. Fan, Heterogeneous nucleation of α-Al grain on primary α-AlFeMnSi intermetallic investigated using 3D SEM ultramicrotomy and HRTEM, Metall. and Mat. Trans. A 45 (2014) 3971–3980.
[41] P. Liang, T. Tarfa, J.A. Robinson, S. Wagner, P. Ochin, M.G. Harmelin, H.J. Seifert, et al., Experimental investigation and thermodynamic calculation of the Al–Mg–Zn system, Thermochim. Acta 314 (1998) 87–110.
[42] J.I. Rojas, D. Crespo, Dynamic microstructural evolution of an Al–Zn–Mg–Cu alloy (7075) during continuous heating and the influence on the viscoelastic response, Mater. Charact. 134 (2017) 319–328.
[43] B. Milkereit, M. Österreich, P. Schuster, G. Kirov, E. Mukeli, O. Kessler, Dissolution and precipitation behavior for hot forming of 7021 and 7075 aluminum alloys, Metals (Basel) 8 (2018) 531.
[44] J.A. Österreicher, G. Kirov, S.S.A. Gerstl, E. Mukeli, F. Grabner, M. Kumar, Stabilization of 7xxx aluminium alloys, J. Alloys Compd. 740 (2018) 167–173.
[45] J.D. Robson, Modelling the overlap of nucleation, growth and coarsening during precipitation, Acta Mater 52 (2004) 4669–4676.
[46] Y. Zhang, C. Bettles, P.A. Rometsch, Effect of recrystallisation on Al3Zr dispersoid behaviour in thick plates of aluminium alloy AA7150, J. Mater. Sci. 49 (2014) 1709–1715.
[47] Y. Zhang, Quench Sensitivity of 7xxx Series Aluminium Alloys. Doctoral thesis, Monash University, Clayton, 2014.

[48] T. Klein, G. Graf, P. Staron, A. Stark, H. Clemens, P. Spoerk-Erdely, Microstructure evolution induced by the intrinsic heat treatment occurring during wire-arc additive manufacturing of an Al-Mg-Zn-Cu crossover alloy, Mater. Lett. 303 (2021) 130500.
[49] B. Dong, X. Cai, S. Lin, X. Li, C. Fan, C. Yang, H. Sun, Wire arc additive manufacturing of Al-Zn-Mg-Cu alloy: microstructures and mechanical properties, Addit. Manuf. 36 (2020) 101447.
[50] E.M. Elgallad, P. Shen, Z. Zhang, X.-.G. Chen, Effects of heat treatment on the microstructure and mechanical properties of AA2618 DC cast alloy, Mater. Des. 61 (2014) 133–140.
[51] M. Kumar, N. Sotirov, C.M. Chimani, Investigations on warm forming of AW-7020-T6 alloy sheet, J. Mater. Process. Technol. 214 (2014) 1769–1776.